

A fluorinated cation introduces new interphasial chemistries to enable high-voltage lithium metal batteries

Received: 7 December 2022

Accepted: 18 April 2023

Published online: 21 June 2023

Check for updates

Qian Liu¹, Wei Jiang², Jiayi Xu¹, Yaobin Xu³, Zhenzhen Yang¹, Dong-Joo Yoo¹, Krzysztof Z. Pupek⁴, Chongmin Wang³, Cong Liu¹, Kang Xu⁵ & Zhengcheng Zhang¹✉

Fluorides have been identified as a key ingredient in interphases supporting aggressive battery chemistries. While the precursor for these fluorides must be pre-stored in electrolyte components and only delivered at extreme potentials, the chemical source of fluorine so far has been confined to either negatively-charge anions or fluorinated molecules, whose presence in the inner-Helmholtz layer of electrodes, and consequently their contribution to the interphasial chemistry, is restricted. To pre-store fluorine source on positive-charged species, here we show a cation that carries fluorine in its structure is synthesized and its contribution to interphasial chemistry is explored for the very first time. An electrolyte carrying fluorine in both cation and anion brings unprecedented interphasial chemistries that translate into superior battery performance of a lithium-metal battery, including high Coulombic efficiency of up to 99.98%, and Li⁰-dendrite prevention for 900 hours. The significance of this fluorinated cation undoubtedly extends to other advanced battery systems beyond lithium, all of which universally require kinetic protection of highly fluorinated interphases.

The lithium-ion battery (LIB) is not only the most popular electrochemical device invented by mankind, but it is also the very first battery relying on interphases, because its electrode materials (graphitic anodes and transition metal oxide cathodes) must operate at potentials far beyond the thermodynamic stability limits of any known electrolytes^{1,2}. The excellent reversibility of modern LIBs, as characterized by thousands of cycles and up to hundred years of calendar life³, is ensured by the interphases that are formed by the sacrificial decompositions of electrolyte components during the initial activation cycles. Although the exact formation mechanism and structure of the interphases remain to be understood, persistent studies on this important sub-component in the past decades have identified the electrolyte solvents (carbonate esters) and salt anions (hexafluorophosphate PF₆⁻ or

tetrafluoroborate BF₄⁻) as the major chemical sources for the interphasial chemistry⁴⁻⁹. More recent investigations have revealed that the fluorides from those anions and solvents might serve as key ingredients in resisting electrochemical reductions and oxidations while providing fast Li⁺-conduction pathways via interfacing with semi-carbonates at nano-length scale¹⁰⁻¹³. Therefore, designing an interphase with enriched, but nanosized fluorides that are evenly distributed in the heterogenous matrices of carbonates, oxides, and polymeric species becomes the central mission of developing better electrolytes for future battery chemistries of high energy densities. Such an interphase would dictate the success of “Holy Grail” batteries based on lithium-metal anode and high capacity, high voltage cathodes, as well as other advanced battery concepts beyond lithium-based chemistries.

¹Chemical Sciences and Engineering Division, Argonne National Laboratory, Lemont, IL 60439, USA. ²Computational Science Division, Argonne National Laboratory, Lemont, IL 60439, USA. ³Environmental Molecular Sciences Laboratory, Pacific Northwest National Laboratory, Richland, WA 99352, USA.

⁴Applied Materials Division, Argonne National Laboratory, Lemont, IL 60439, USA. ⁵Battery Science Branch, Energy Science Division, Sensor and Electron Devices Directorate, U.S. Army Research Laboratory, Adelphi, MD 20783, USA. ✉ e-mail: conrad.k.xu.civ@army.mil; zzhang@anl.gov

Despite the various efforts of fluorinating the interphases, including the most recent super-concentrated^{14–16} or locally-concentrated electrolytes^{17–23} as well as all-fluorinated electrolytes^{24–28}, the chemical sources of these interphasial fluorine formed in all the investigated electrolytes have been restricted to two classes of species: (1) the fluorinated salt anions (PF_6^- , BF_4^- , or the newly developed bis(trifluoromethanesulfonyl)imide, TFSI⁻, or bis(fluorosulfonyl)imide, FSI⁻) that bear negative charge and (2) fluorinated solvent molecules that bear no charge. This restricted source brings an intrinsic disadvantage to the desired chemistry of interphases, because these fluorinated precursors could not populate the inner-Helmholtz layers of the electrode surface of a high Fermi energy level, such as Li^0 anode, hence their participation in the interphasial chemistry thereon was consequently handicapped. Such a disadvantage can be most visibly evidenced in the so-called “cathodic challenge” encountered in the efforts of protecting anode surfaces in aqueous electrolytes, because in that case the interphasial chemistry would completely rely on the contributions from anion reduction^{29–31}. Beside the charge of these fluorine precursors, the nature of the fluorine bonds also matters, as the C–F bonds seem to provide higher quality interphasial fluorination than the labile fluorines sitting on heteroatoms, such as phosphorus, boron, or sulfur^{32,33}. Hence, in the broader context, a cation bearing C–F bonds is a highly coveted structure, because its presence, along with fluorinated anions and solvent molecules, would ensure maximum and balanced fluorination of interphases on both anode and cathode surfaces.

In this work, we successfully synthesized a fluorinated cation, 1-methyl-1-propyl-3-fluoropyrrolidinium and apply this F-cation concept on interphase in high-voltage Li-metal batteries for the first time. When coupled with a fluorinated anion FSI⁻, it forms an ionic liquid (PMpyr_FFSI) that has zero vapor pressure, has complete non-flammability, and carries potential fluorine sources on both cation and anion. Lithium salt with the same anion (LiFSI) can dissolve in this ionic liquid at various concentrations, leading to an ionic liquid electrolyte that offers unprecedented interphasial chemistry opportunities when the

electrolyte interacts with both cathode and anode of the two extreme potentials.

Results and discussion

Electrolyte stability

PMpyr_FFSI containing one fluorine in the pyrrolidinium cation ring was synthesized through a one-step quaternization method with methyl bis(fluorosulfonyl)imide (MeFSI) as the methylating agent with 100% conversion (Fig. 1a, b). Density function theory (DFT) calculations reveal that, in comparison with non-fluorinated counterpart, 1-methyl-1-propylpyrrolidinium (PMpyr⁺), the presence of fluorine reduces the energy levels of both HOMO (from -13.18 to -13.29 eV) and LUMO (from -3.47 to -3.66 eV) of the cation (Fig. 1a). Such down shift in HOMO/LUMO energy indicates the increased resistance of the cation against oxidation but also shows lowered resistance against reduction³⁴. Consistent with HOMO energy calculation by DFT, PMpyr_FFSI shows good anodic stability up to 5.5 V vs. Li^+/Li in cyclic voltammetry test, which is slightly higher than the 5.4 V for PMpyrFSI³⁵. Moreover, the higher oxidation stability of PMpyr_FFSI is even manifest from the potentiostatic hold experiment conducted at higher voltages from 4.6 to 4.9 V, as it exhibits lower leakage current compared to PMpyrFSI (Supplementary Fig. S1).

Potential energy surfaces were also constructed based on DFT calculations. The pyrrolidinium cation, either with or without the fluorine, binds equally strong to Li^0 surface (-2.12 and -2.10 eV, respectively), but much stronger than the FSI⁻ anion (-0.66 eV). However, PMpyr_F⁺ undergoes reductive decomposition with C–F cleavage, which is exothermic by -3.67 eV, as compared with C–H cleavage that is exothermic by -0.26 eV, followed by the ring-opening process, which is exothermic by -0.87 eV (Fig. 1c). Therefore, the introduction of fluorine renders the reduction of PMpyr_F⁺ much more favored than PMpyr⁺, while such difference in reactivity is primarily due to the strong interaction between the F and Li (110) surface. As indicated by the density of states (Supplementary Fig. S3), the significant orbital overlapping between Li-p orbital and F-s and p

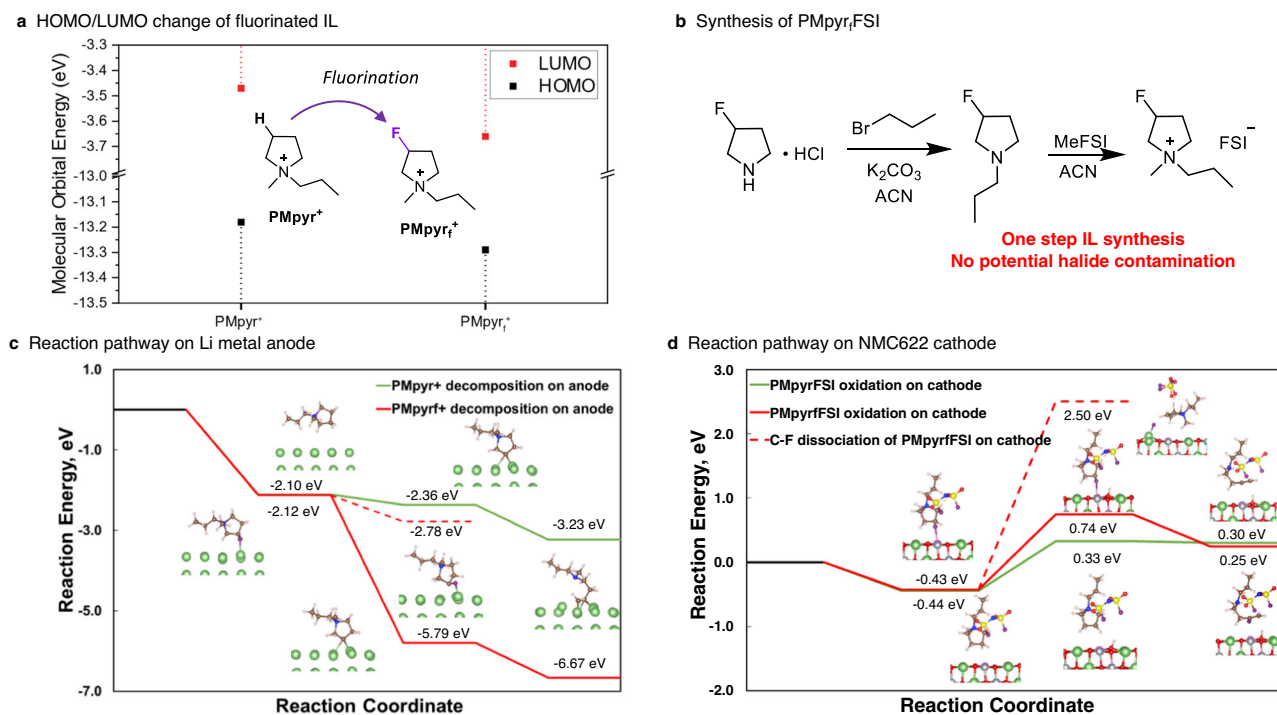


Fig. 1 | Synthesis and DFT calculations of fluorine substituted cation PMpyr_F⁺. **a** Comparison of HOMO/LUMO energy levels for PMpyr_F⁺ and PMpyr⁺. **b** Synthesis route for PMpyr_FFSI. **c** PMpyr_F⁺ and PMpyr⁺ reduction pathway on Li metal. **d** PMpyr_F⁺ and PMpyr⁺ oxidation pathway on NMC622 cathode.

orbitals indicates the strong interaction. However, the orbital overlapping cannot be found for H interacting with the Li (110) surface. The strong interaction between F and Li (110) surfaces makes C–F cleavage more energetically favorable than C–H cleavage by -3.41 eV, which would preferentially generate inorganic or organic fluorides. Deprotonation pathway was also considered for the PMpyr_f^+ cation decomposition, this mechanism is exothermic by -0.66 eV (Fig. 1c, red dash line). In comparison with PMpyr^+ cation, the deprotonation becomes more thermodynamically favored (-0.66 vs. -0.26 eV), which could be due to the presence of electron-withdrawing F that weakens the C–H bond that shares the same carbon. This demonstrated that deprotonation could also participate in SEI formation, however, the defluorination is the dominating pathway. Meanwhile, the FSI^- decomposition is also highly likely (Supplementary Fig. S2b), as evidenced by the exothermic S–F bond cleavage of -5.97 eV, followed by exothermic dissociation of S–O bond, which is -2.94 eV. The fluorides thus generated from the labile bonds in FSI^- would more likely exist in inorganic forms with heteroatom contents (P, S) and behave less protectively as the fluorides generated from C–F bonds³⁶. To mimic the decomposition during charge state, the potential energy surface with consideration of e^- transfer after adsorption is constructed and shown in Supplementary Fig. S2a, S2b. The reaction energy for the FSI^- , PMpyr_f^+ , and PMpyr^+ activations are -6.82 , -6.55 , and -3.14 eV, respectively. Thus, the corresponding reduction potentials are 5.43, 5.16, and 1.75 V, according to Eq. (1) in “Methods”. In a nutshell, the cations bind to the Li (110) surface much stronger than anions do; however, without F-substitution, PMpyr^+ are not as active as FSI^- toward reduction. With F-substitution, PMpyr_f^+ is more active towards reduction in comparison with PMpyr^+ and is almost as active as FSI^- anion. Fortunately, the higher adsorption preference of PMpyr_f^+ over FSI^- should lead to more abundant fluorides from C–F origin—due to the fluorinated cation.

On the NMC622 cathode side, PMpyrFSI and PMpyr_fFSI bind equally strong with Mn sites through the cation part with cation adsorption energy of 0.44 eV and 0.43 eV, respectively; however, the adsorption is much weaker when binding through anion part (0.39 eV). Therefore, we will only consider cation oxidation during the charging cycle. As indicated by Fig. 1d, PMpyr_fFSI oxidation favors a deprotonation rather than a C–F dissociation pathway, due to the lower potential energy for deprotonation compared with C–F cleavage (1.17 eV vs 2.93 eV). Furthermore, the C–N bond is weakened, followed by a ring-opening process of deprotonated PMpyr_fFSI , which results in a potential energy of -0.49 eV. However, in the absence of fluorine, PMpyrFSI tends to be more easily oxidized with reaction potential energy of 0.77 eV for the deprotonation step, followed by the exothermic ring-opening process of -0.03 eV. This indicates that F-substitution indeed renders PMpyr_fFSI more resistant against oxidation, as predicted by the downshift of HOMO/LUMO energy. Apparently, what was brought by fluorination is the improvement in thermodynamic stability against oxidation on cathode surfaces, as well as a strong tendency to decompose on the Li^0 anode. As we have learned from the knowledge in LIB electrolytes, the latter strongly implies the preferential cation reduction to form interphases on Li^0 .

An ionic electrolyte $(\text{PMpyr}_f)_{0.8}\text{Li}_{0.2}\text{FSI}$ was formulated by dissolving LiFSI in PMpyr_fFSI , whose performance was evaluated in a lithium-metal cell consisting of NMC622 cathode and a thin (20 μm) lithium anode. Molecular dynamics (MD) simulation sheds light on the electrode/electrolyte interfacial structure in such batteries. Compared with its non-fluorinated cousin, the fluorine presence on the cation (purple) makes it much easier to access and populate the inner-Helmholtz layers on both the NMC622 cathode and Li-metal anode (Fig. 2a, b), which suggests stronger surface interaction of PMpyr_f^+ cation with those electrode surfaces and predicts an interphalial chemistry with higher participation from PMpyr_f^+ . The same insight was provided from the static distribution of the electrolyte

components on both electrodes (Fig. 2d, e). On both Li^0 and NMC622 cathode surfaces, the PMpyr_f^+ cations are much more populated within the inner-Helmholtz layer than its counterpart PMpyr^+ without fluorine.

Performance in battery

Although fluorination of the cation favors the desired interfacial structure and interphalial chemistry of high fluorine abundance, excess PMpyr_f^+ content in the electrolyte does increase bulk viscosity and leads to lower ion transport and higher interfacial impedance (Supplementary Fig. S4). Therefore, we must further optimize the electrolyte formulation by considering the impact of interfacial impedance (Supplementary Fig. S9a). Different from neutral organic solvent-based electrolytes, where Li^+ ion is solvated by both solvent molecules and Li salt anion, Li^+ ion in pure ionic liquid-based electrolytes is solely solvated by anions and ionic liquid cation does not participate in Li^+ ion solvation. Optimization of the PMpyr_f^+ concentration in the inner-Helmholtz layer can be achieved by adjusting Li^+ concentration in the format of lithium salt. The $(\text{PMpyr}_f)_{0.5}\text{Li}_{0.5}\text{FSI}$ electrolyte is the composition that better balances these considerations. At this composition, the interfacial structure, as well as the static distribution of the electrolyte components, becomes less adsorbed on both electrode surfaces (Fig. 2c, f). Instead, more Li^+ (green) are observed on both electrode surfaces, and the purple F-group from PMpyr_f^+ cation is reduced, especially on the Li-metal surface.

The electrolyte interfacial structure alteration causes corresponding changes in solid–electrolyte–interphase (SEI) and cathode–electrolyte–interphase (CEI) chemistries, which are revealed by X-ray photoelectron spectroscopy (XPS) analysis. On a Li-metal surface (Fig. 3a), peaks observed in $F 1s$ spectra are assigned to be SO_2F at 687.8 eV, C–F at 686.5 eV and LiF at 684.5 eV, where SO_2F is contributed from FSI^- decomposition, C–F is contributed from PMpyr_f^+ cation, and LiF is contributed from both FSI^- decomposition and PMpyr_f^+ cation defluorination. Peaks observed in $N 1s$ spectra are assigned to be $\text{N-SO}_2\text{F}$ (FSI^- decomposition) at 400.6 eV, C– N^+ (PMpyr_f^+ cation decomposition) at 402.3 eV and LiNC_xH_y (PMpyr_f^+ cation decomposition via ring-opening mechanism) at 399.2 eV. At decreased PMpyr_f^+ concentration, the peak relative intensity of 402.3 eV is decreased and 399.2 eV is increased in $N 1s$ spectra for $(\text{PMpyr}_f)_{0.5}\text{Li}_{0.5}\text{FSI}$ electrolyte, suggesting PMpyr_f^+ contribution to the SEI is mainly through the ring-opening mechanism, which also contributes to higher LiF content as observed in $F 1s$ spectra. Moreover, lower C atomic concentration and higher S atomic concentration are observed in $(\text{PMpyr}_f)_{0.5}\text{Li}_{0.5}\text{FSI}$ electrolyte, suggesting reduced PMpyr_f^+ cation decomposition on Li metal, as C should have solely come from the cation and S from the FSI^- anion, respectively. This shift of interphalial chemistry between PMpyr_f^+ cation and FSI^- anion is apparently a result of PMpyr_f^+ cation reduction in interfacial region. On NMC622 cathode, a similar trend is observed, in which the intensities of the C–F peak and C–N peaks contributed from PMpyr_f^+ cation decomposition are relatively lower. A peak at 529.2 eV is assigned to metal oxide (M–O) species in $O 1s$ spectrum for $(\text{PMpyr}_f)_{0.5}\text{Li}_{0.5}\text{FSI}$ electrolyte, suggesting that the cathode surface is visible now through the formation of a thinner CEI layer (Supplementary Fig. S8). Supporting this argument, both N and S are also observed in lower atomic concentration because of less cation and anion decomposition overall. While both PMpyr_f^+ cation and FSI^- anion participate in the SEI formation on the Li-metal anode and CEI formation on NMC622 cathode, the contribution between cation and anion needs to be balanced to enable optimized interphalial chemistry, which can be achieved by adjusting the cation concentration, and the impact of PMpyr_f^+ cation concentration is more significant on Li metal due to the stronger Coulombic interaction.

The $(\text{PMpyr}_f)_{0.5}\text{Li}_{0.5}\text{FSI}$ electrolyte was then tested in a NMC622/Li-20 μm cell (designated as full cell hereafter) cycled between 4.6 and

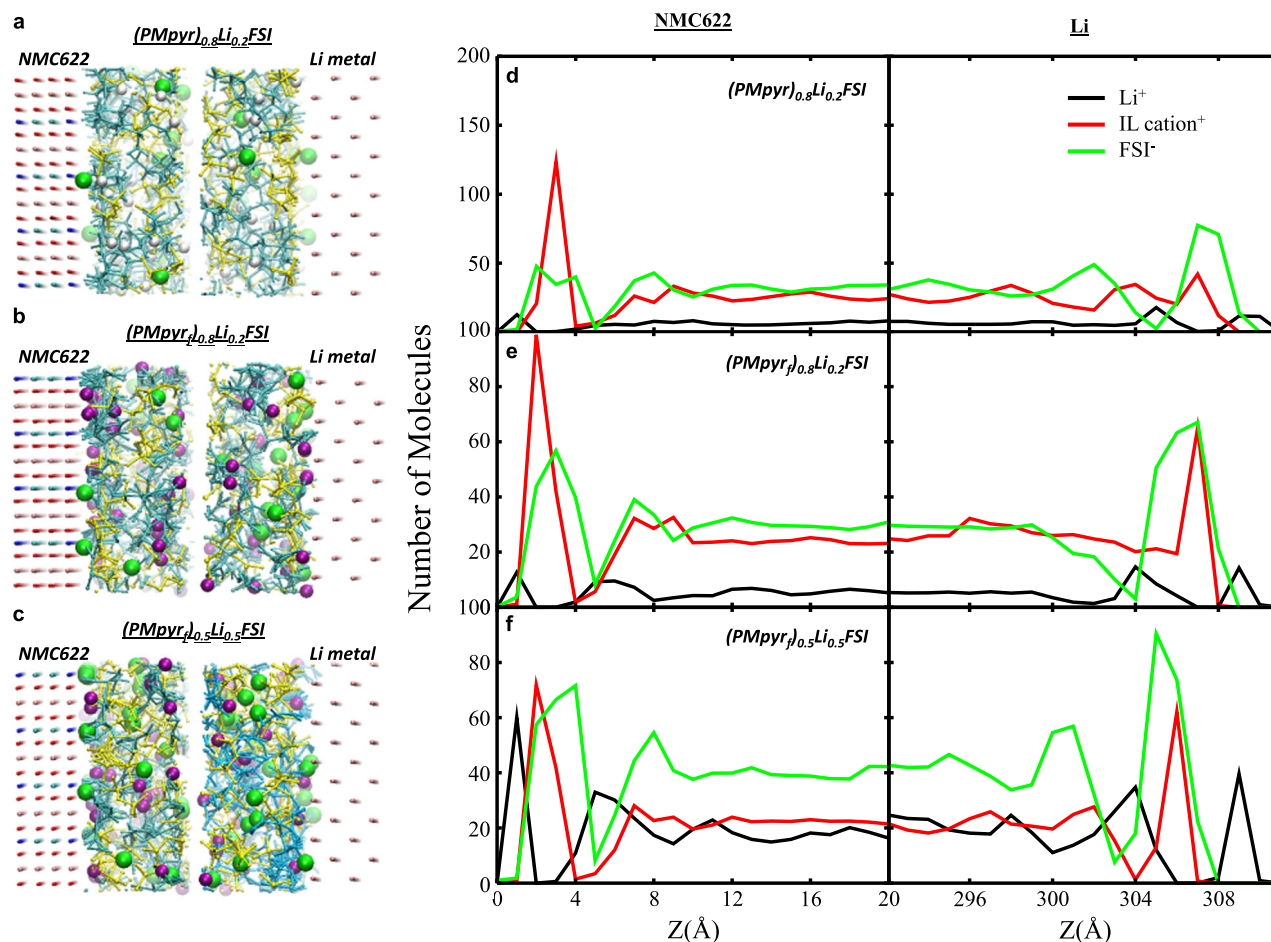


Fig. 2 | MD simulation on electrolyte/electrode interaction. a–c Snapshot of electrolyte distribution on NMC622 and Li electrodes: cyan-IL cation⁺; white-H on the PMpyr⁺ backbone highlight in Fig. 1b; purple-F on the PMpyr⁺ backbone; yellow-FSI⁻; green-Li⁺. d–f Molecular number density profiles along the z-axis

normal to the surface of the NMC cathode (left panels) and lithium anode (right panels). The center of mass of each molecule is used to calculate molecule distribution: a, d (PMpyr)_{0.8}Li_{0.2}FSI electrolyte, b, e (PMpyr)_{0.8}Li_{0.2}FSI electrolyte and c, f (PMpyr)_{0.5}Li_{0.5}FSI electrolyte.

3.0 V (N/P ratio is around 2). Despite its higher room-temperature viscosity (528 mPa s)³⁵, (PMpyr)_{0.5}Li_{0.5}FSI delivers a much higher initial discharge capacity of 203 mAh/g at C/3, as compared to 147 mAh/g for (PMpyr)_{0.8}Li_{0.2}FSI (Fig. 4a). This capacity was well-retained, with only 3 mAh/g lost during the first 100 cycles, at an average coulombic efficiency (CE) of 99.9%. The rate capability for (PMpyr)_{0.5}Li_{0.5}FSI electrolyte is also superior to (PMpyr)_{0.8}Li_{0.2}FSI electrolyte, as evaluated in NMC622/Li-450 μm cell (designated as half-cell hereafter) with 4.6 V upper cutoff voltage (UCV). Although the impedance contributed from (PMpyr)_{0.5}Li_{0.5}FSI is around 57 Ω cm², which is much higher than 16 Ω cm² for (PMpyr)_{0.8}Li_{0.2}FSI due to the viscosity impact, the overall surface impedance is only 85 Ω cm² for (PMpyr)_{0.5}Li_{0.5}FSI, substantially lower than 231 Ω cm² for (PMpyr)_{0.8}Li_{0.2}FSI after three formation cycles (Supplementary Fig. S9a) and consistent with the observed cycling and rate performance. The enhanced cycling and rate performance and lower surface impedance are attributed to the balanced cation and anion contributions to the CEI and SEI chemistries. The full-cell cycling with (PMpyr)_{0.5}Li_{0.5}FSI electrolyte was further extended to 300 cycles (Fig. 4c). High-capacity retention of 89% is achieved for 300 cycles, with minimum overpotential buildup (Supplementary Fig. S9e). After 300 cycles, the surface impedance in (PMpyr)_{0.5}Li_{0.5}FSI electrolyte cell is only slightly increased (Supplementary Fig. S9b), in contrast with the conventional electrolyte Gen 2 (1.2 M LiPF₆ in EC/EMC 3/7 weight ratio), which could initially deliver 220 mAh/g capacity at C/3 rate due to its lower viscosity and high conductivity (7.5 mS/cm at 25 °C), but rapidly fades due to its low

oxidation stability on the cathode and the poor stability towards the Li-metal anode.

The half-cell performance at 4.6 V was also evaluated with Gen 2 and (PMpyr)_{0.5}Li_{0.5}FSI electrolyte (Supplementary Fig. S10a). By supplying the cell with an unlimited Li source, we can examine the electrolytes high-voltage performance without the Li-metal factor. The cycling performance of Gen 2 is much improved under such a circumstance, with similar fading patterns to the first 30 cycles in the Gen 2 full-cell performance, which is mainly due to the cathode-side degradation. Again, a stable cycling is achieved by (PMpyr)_{0.5}Li_{0.5}FSI electrolyte in the half-cell. These results suggest that a good NMC622 surface protection is enabled by (PMpyr)_{0.5}Li_{0.5}FSI electrolyte. The nearly identical cycling performance for (PMpyr)_{0.5}Li_{0.5}FSI electrolyte in both half and full-cells within 100 cycles also indicates its high Li-metal compatibility. The (PMpyr)_{0.5}Li_{0.5}FSI electrolyte also demonstrates stable cycling performance under different UCV, as shown in Supplementary Fig. S9b–S9d. The great cyclability of (PMpyr)_{0.5}Li_{0.5}FSI electrolyte compared to the conventional electrolyte suggests this electrolyte has high-voltage stability on the Ni-rich cathode and high Li-metal compatibility. More importantly, the results indicate the modified CEI and SEI are highly protective against further electrolyte degradation over long-term cycling.

Stabilization of Li metal

The high stability of (PMpyr)_{0.5}Li_{0.5}FSI toward Li metal was further confirmed in Li/Cu cells and Li/Li symmetric cells. The CE of Li-metal

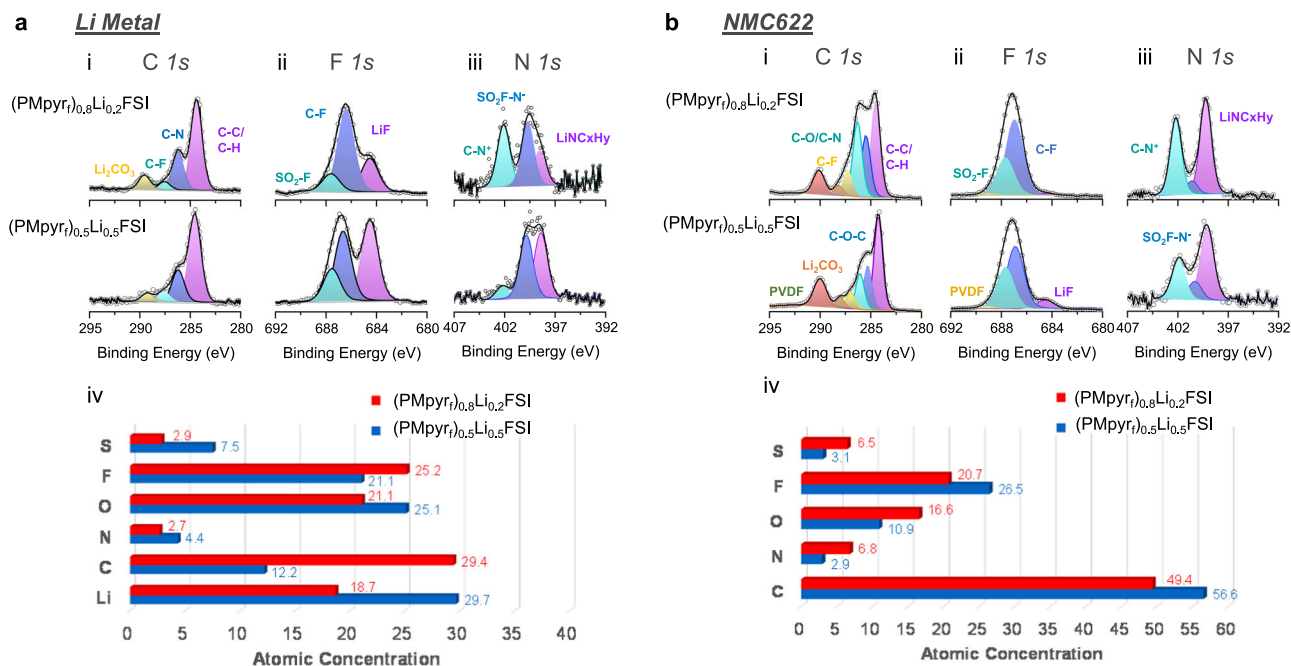


Fig. 3 | XPS analysis of recovered electrodes. a Li-metal anode and **b** NMC622 cathode harvested after formation using (PMpyr)_{0.8}Li_{0.2}FSI and (PMpyr)_{0.5}Li_{0.5}FSI electrolytes. (i) C 1s spectra, (ii) F 1s spectra, (iii) N 1s spectra, and (iv) atomic concentration.

anode cycling is measured in Cu/Li cells using Aurbach CE Protocol³⁷ with Gen 2, (PMpyr)_{0.8}Li_{0.2}FSI and (PMpyr)_{0.5}Li_{0.5}FSI electrolytes at current density of 0.1 mA/cm² (Fig. 5a–c). Gen 2 electrolyte consumes all Li inventory within only three cycles and displays a low CE of 45.0%. Both PMpyr_FFSI-based electrolytes demonstrated substantially higher CE, with (PMpyr)_{0.5}Li_{0.5}FSI showing a higher CE of 97.9% compared to 96.5% for (PMpyr)_{0.8}Li_{0.2}FSI. Similar performance is also observed in long-term cycling of Li/Cu cells (Fig. 5d). Li was plated on to Cu foil for 6 h and stripped to 1 V for 100 cycles with 0.1 mA/cm² current density. Gen 2 electrolyte shows lower than 35% CE throughout 100 cycles, while (PMpyr)_{0.8}Li_{0.2}FSI and (PMpyr)_{0.5}Li_{0.5}FSI show high CE of 99% after initial stabilization. With decreased PMpyr⁺ cation concentration, (PMpyr)_{0.5}Li_{0.5}FSI shows a higher first cycle CE than (PMpyr)_{0.8}Li_{0.2}FSI, which suggests the SEI formed by (PMpyr)_{0.5}Li_{0.5}FSI electrolyte is thinner and more efficiently protects the Li surface from further degradation.

Gen 2, (PMpyr)_{0.8}Li_{0.2}FSI and (PMpyr)_{0.5}Li_{0.5}FSI electrolytes were also examined in Li/Li symmetric cells (Fig. 5e and Supplementary Fig. S11). For Gen 2 electrolyte, after the initial stabilization, the overpotential continues to increase and starts to polarize after 700 h, which correlates to the undesired side reactions between the Gen 2 electrolyte and Li metal, which results in the accumulation of SEI layer, impedance buildup, and electrolyte depletion. The voltage profile also demonstrates a characteristic “peaking” behavior (Supplementary Fig. S11a) that is ascribed to different resistances of dendrite formation (nucleation), dendrite dissolution, bulk dissolution, and pitting from bulk Li surface³⁸. This type of voltage trace is typically correlated to a dendritic morphology on a Li surface (Fig. 6a). For (PMpyr)_{0.8}Li_{0.2}FSI electrolyte, the initial overpotential is slightly higher compared to (PMpyr)_{0.5}Li_{0.5}FSI electrolyte, regardless of its lower viscosity, which suggests the excessive SEI formed by the fluorinated cation in (PMpyr)_{0.8}Li_{0.2}FSI electrolyte has higher surface impedance. The overpotential continues decreases over cycling and cell experienced soft shorting issue after 600 h. This result is consistent with the higher portion of dendritic morphology observed in plated Li on Cu foil with (PMpyr)_{0.8}Li_{0.2}FSI electrolyte (Fig. 6b). For (PMpyr)_{0.5}Li_{0.5}FSI electrolyte, the voltage profile is stable over 900 h, which indicates that SEI formed by (PMpyr)_{0.5}Li_{0.5}FSI sufficiently protects the Li-metal surface

and minimizes the undesired side reactions under the current testing condition. The stable overpotential also suggests that the Li surface area is relatively maintained during Li plating/stripping process, which could be due to the more densely packed columnar Li morphology in (PMpyr)_{0.5}Li_{0.5}FSI electrolyte, as shown in Fig. 6c. The voltage profiles of (PMpyr)_{0.8}Li_{0.2}FSI and (PMpyr)_{0.5}Li_{0.5}FSI show the “arcing” behavior corresponding to a diffusion-controlled process (Supplementary Fig. S11b, c). The excellent Li-metal compatibility with (PMpyr)_{0.5}Li_{0.5}FSI is further demonstrated by Li/Li symmetric cell using a thin Li foil of 20 μm. (PMpyr)_{0.5}Li_{0.5}FSI exhibits stable voltage profile over 500 h testing, while Gen 2 polarizes within 50 h testing due to Li source being exhausted (Supplementary Fig. S11e, f). PMpyr_FFSI-based electrolytes show high Li-metal compatibility as demonstrated in both Li/Cu and Li/Li cells, which could be contributed by the SEI formed by both PMpyr⁺ cation and FSI⁻ anion. Moreover, with the PMpyr⁺ cation concentration optimization, the SEI formed by (PMpyr)_{0.5}Li_{0.5}FSI electrolyte shows lower impedance, which enables uniform and highly densely packed Li morphology during Li plating.

Protection of NMC622 surface

Cycled NMC622 was recovered from the cycled half-cells for surface morphology and chemical structure analysis. High-resolution transmission electron microscopy (STEM) reveals a difference in the surface structure change (Fig. 7) with electrolytes. Previous studies have shown that, while the cathode degradation is mainly incurred by its intrinsic structural instability, the process usually starts at the cathode/electrolyte interface. Thus, a well-maintained layered surface structure after cycling confirms the efficacy of a protective CEI, which extensively suppresses the side reactions from propagating^{39–41}. For NMC622 recovered from Gen 2 electrolyte, a thick surface rock-salt layer (~6 nm) is observed, with a 2-nm-thick CEI, and cracks inside the primary particles are observed. Such excessively thin CEI borders on the lower limit for interphases, as electron tunneling could easily occur. An electron energy loss spectroscopy (EELS) line scan was conducted from the primary particle surface to the bulk. The O-K pre-peak is much weaker at primary particle surface compared to bulk, suggesting more oxygen vacancies formed near surface. This result is

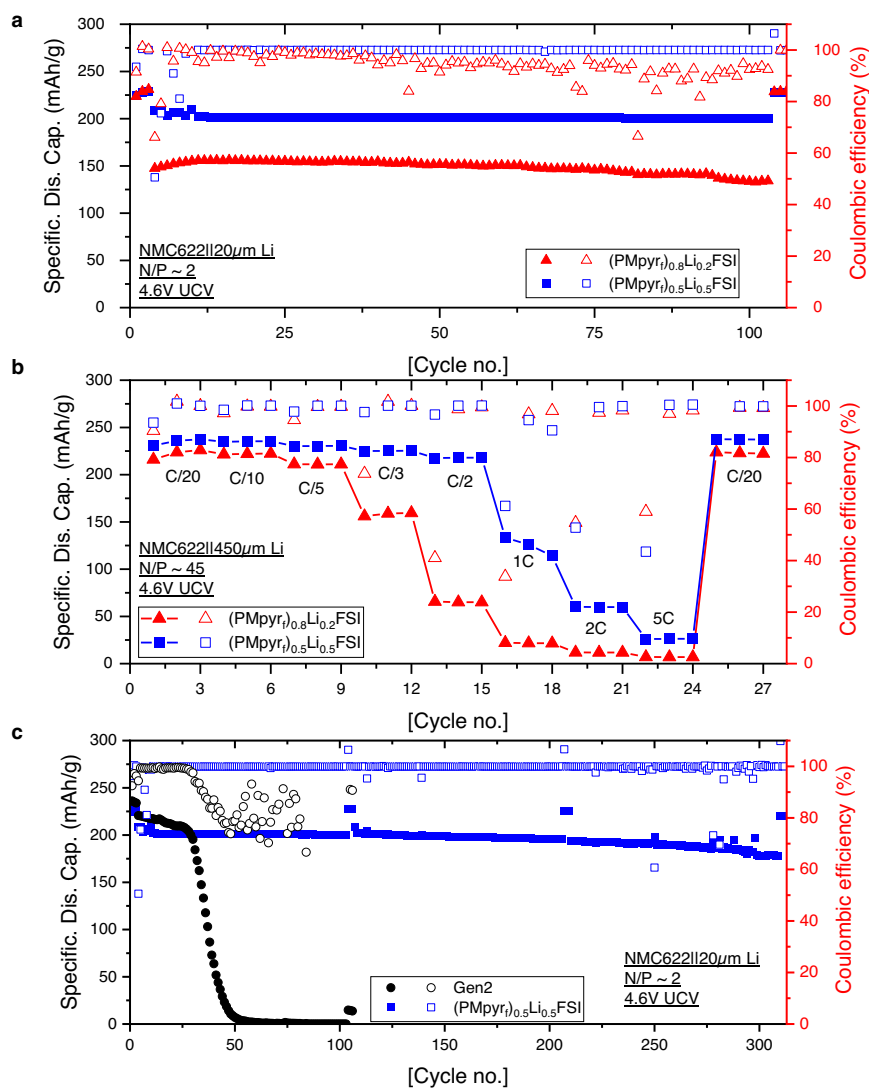


Fig. 4 | NMC622/Li cell performance. **a** Full-cell performance cycled using $(\text{PMpyr})_{0.8}\text{Li}_{0.2}\text{FSI}$ and $(\text{PMpyr})_{0.5}\text{Li}_{0.5}\text{FSI}$ electrolytes. **b** Rate capability of $(\text{PMpyr})_{0.8}\text{Li}_{0.2}\text{FSI}$ and $(\text{PMpyr})_{0.5}\text{Li}_{0.5}\text{FSI}$ electrolytes cycled in half-cell. **c** Long-

term cycling performance for full cell using Gen 2 and $(\text{PMpyr})_{0.5}\text{Li}_{0.5}\text{FSI}$ electrolytes. Cutoff voltage for all NMC622/Li cells is 4.6–3.0 V.

consistent with poor high-voltage performance in Gen 2 electrolyte and high surface impedance, as shown in Supplementary Fig. S9a. As the CEI formed by Gen 2 electrolyte cannot fully protect the NMC surface, electrolyte oxidation continues during high-voltage cycling, resulting in surface O loss and persistent phase transition from layer to resistive rock-salt structure^{42–47}. For $(\text{PMpyr})_{0.8}\text{Li}_{0.2}\text{FSI}$ electrolyte, no inner granular cracking was observed in the primary particle even after 100 cycles. A thick CEI layer of 8 nm is observed, suggesting more electrolyte decomposition on the surface that provides sufficient protection against electron tunneling, but meanwhile introduces excessive interfacial impedance to Li^+ -migration. The cation mixing layer observed on the surface is rather thin. The EELS line scan shows a very low signal at 5 nm depth correlating under this thick CEI. The pre-peaks observed from 10 nm are very similar to the bulk, suggesting that the CEI formed by $(\text{PMpyr})_{0.8}\text{Li}_{0.2}\text{FSI}$ is thick enough to prevent cathode surface degradation. The most striking difference is observed for the $(\text{PMpyr})_{0.5}\text{Li}_{0.5}\text{FSI}$ electrolyte cycled cathode. At decreased cation concentration, NMC cathode cycles only shows about a 2-nm surface transition layer (Fig. 7d), which is only 1 nm thicker compared to pristine NMC sample (Fig. 7a), while the interfacial impedance is much lower, as shown in Supplementary Fig. S9. No intra- or inter-granular cracking is observed, and after 300 cycles, the CEI is only

about 1 nm thick, and the EELS line scan shows similar pre-peaks from surface to bulk. These results indicate that the CEI formed by $(\text{PMpyr})_{0.5}\text{Li}_{0.5}\text{FSI}$ is fairly thin, while its chemistry renders it highly protective, which minimized the oxidation reaction on the electrolyte/cathode interface, suppressed the O loss on the cathode surface, and preserved the layer structure. Apparently, the $(\text{PMpyr})_{0.5}\text{Li}_{0.5}\text{FSI}$ electrolyte achieved a proper balance of providing sufficient protection of the cathode surface while minimizing resistance to ion transport.

In summary, we have demonstrated a fluorinated cation and its impact on interphasial chemistries for the first time in a high-voltage lithium-metal battery. The fluorination brings unique interfacial structure and subsequent interphasial chemistries on both Li^0 anode and high nickel cathode. By optimizing cation concentration in inner-Helmholtz layer, the strong electrode/cation surface interaction caused by fluorination can be attenuated and its optimal interphasial contribution can be achieved, which leads to high Coulombic efficiency, densely packed Li morphology, and excellent cycling stability of the 4.6 V lithium-metal battery. STEM demonstrated that a highly protective CEI formed by $(\text{PMpyr})_{0.5}\text{Li}_{0.5}\text{FSI}$ electrolyte maintains a thin cation mixing layer with minimum surface structure change. The new cation that carries fluorine will cast significant impact on

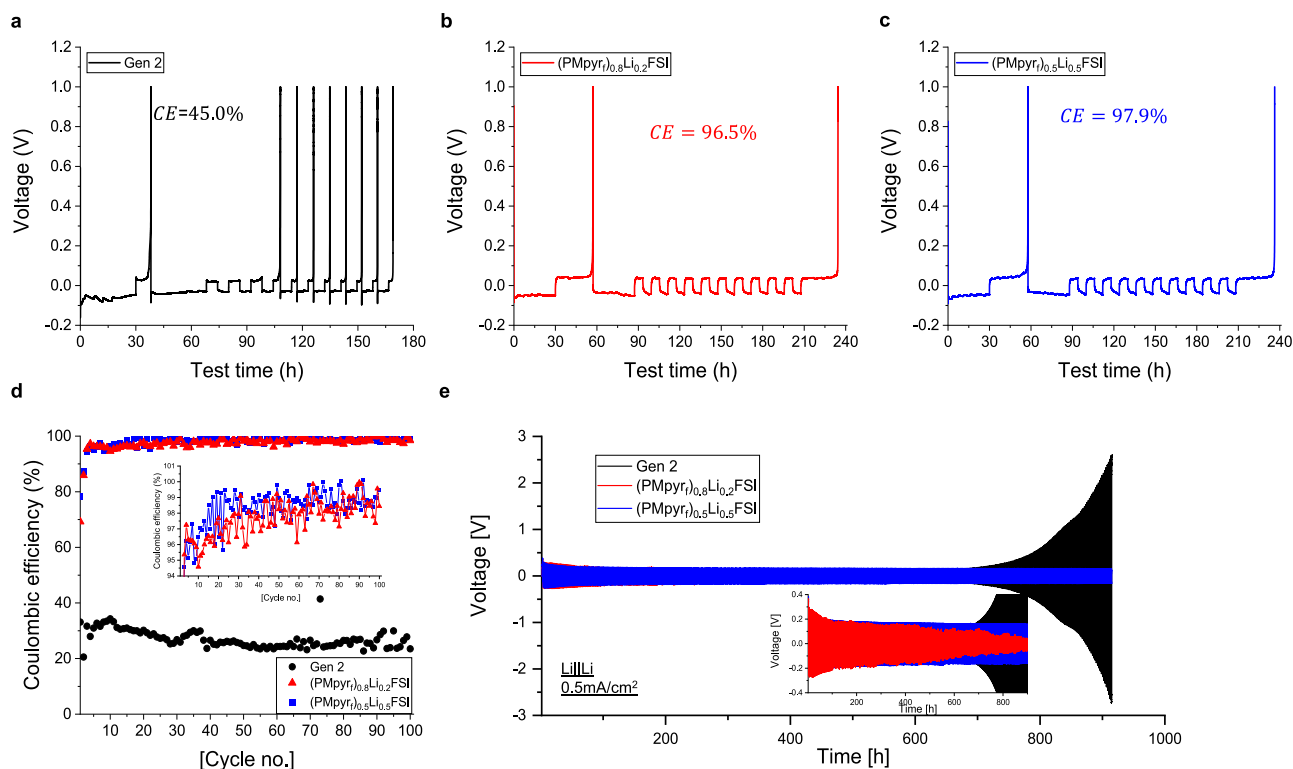


Fig. 5 | Li/Cu and Li/Li symmetric cell performance. **a–c** Voltage profile of an Aurbach test using **a** Gen 2, **b** (PMpyr)_{0.8}Li_{0.2}FSI, and **c** (PMpyr)_{0.5}Li_{0.5}FSI. **d** Coulombic efficiency of Li/Cu cell cycled with current density of 0.1 mA/cm². **e** Voltage profile of Li/Li symmetric cell with current density of 0.5 mA/cm².

emerging battery chemistries that desperately need tailored interphasial chemistries.

Methods

Electrode and electrolyte preparation

LiNi_{0.6}Mn_{0.2}Co_{0.2}O₂ cathode (90% NMC622, Toda Kogyo Corp.; 5% C45 conductive carbon, Timcal; 5% PVDF, Solvay 5130) was fabricated by the CAMP Facility at Argonne National Laboratory. Active material loading is 8.8 mg/cm²e. 1-Methyl-1-propyl-3-fluoropyrrolidinium bis(fluorosulfonyl)imide (PMpyr_rFSI) was synthesized following the literature procedure³⁵ by the one-step reaction of 1-propyl-3-fluoropyrrolidine with MeFSI. The resultant ionic liquid was dried in a lyophilizer for at least two days, then stored in 4 Å molecular sieves and filtered before use. The water content was <20 ppm, measured by Karl–Fischer titrator C30. (PMpyr)_{0.8}Li_{0.2}FSI and (PMpyr)_{0.5}Li_{0.5}FSI electrolytes were prepared by dissolving LiFSI (Nippon Shokubai Co., Ltd.) in PMpyr_rFSI with 4/1 and 1/1 molar ratio in an argon-filled glovebox.

Physical and electrochemical properties

Electrochemical impedance spectroscopy (EIS) measurements were conducted on the Solartron Analytical 1400 Cell test station. Cell impedance was measured with the frequency range from 1 MHz to 0.1 Hz at the open circuit potential.

Galvanostatic charge-discharge cycling tests were conducted on the Maccor Electrochemical Analyzer (MIMSciEnt) with Al-coated 2032-coin cells. NMC622/Li cells were tested with a cutoff voltage of 4.6–3.0 V. Li/Li symmetric cells and Li/Cu cells were assembled using 450-μm-thick Li foil. The separator was a glass micro-fiber disc, and the total electrolyte amount is 100 μL. Cell testing was conducted at 30 °C. For the C-rate test, C/20 was used as charging current, and different currents were used for discharge for three cycles. Aurbach test: 3 mAh/cm² Li reservoir is plated on the Cu foil using 0.1 mA/cm², then

0.6 mAh/cm² Li was stripped/plated for ten cycles before completely stripped to 1 V.

X-ray photoelectron spectroscopy (XPS)

XPS analysis was conducted on a PHI 5000 VersaProbe II system (Physical Electronics) with a base pressure of $\sim 2 \times 10^{-9}$ torr. The spectra were obtained using an Al K α radiation ($h\nu = 1486.6$ eV) beam (100 μm, 25 W), with Ar⁺ and electron beam sample neutralization, in Fixed Analyzer Transmission mode with a pass energy of 11.75 eV. Subtracting a Shirley background and then fitting the spectra to multiple Gaussian peaks was performed on all spectra using the Multipack software from Physical Electronics. The area under the XPS peaks (the sum of the Gaussian components) was adjusted using manufacturer-calibrated relative sensitivity factors and normalized to obtain elemental concentrations. The same normalization factors were used to plot XPS signal intensities as concentration per unit energy (at % eV⁻¹). Binding energy was calibrated by shifting every region to align the C 1s peak of C–C/C–H environments at 284.8 eV.

Scanning electron microscopy and transmission electron microscopy (SEM/TEM)

The cycled coin cells were disassembled in the argon-filled glovebox, and the electrodes were thoroughly rinsed with anhydrous dimethyl carbonate and allowed to air-dry. The morphologies and the elemental mapping of the cycled electrodes were examined using SEM and energy-dispersive X-ray spectroscopy (EDS) using the JOEL JCM-6000-PLUS. TEM analysis was conducted in the JOEL JEM-2100F.

Density functional theory methods

Periodic spin-polarized DFT calculations were performed using the plane-wave-based Vienna ab initio Simulation Package (VASP)⁴⁸. The projector-augmented wave (PAW) method⁴⁹ was used to describe the

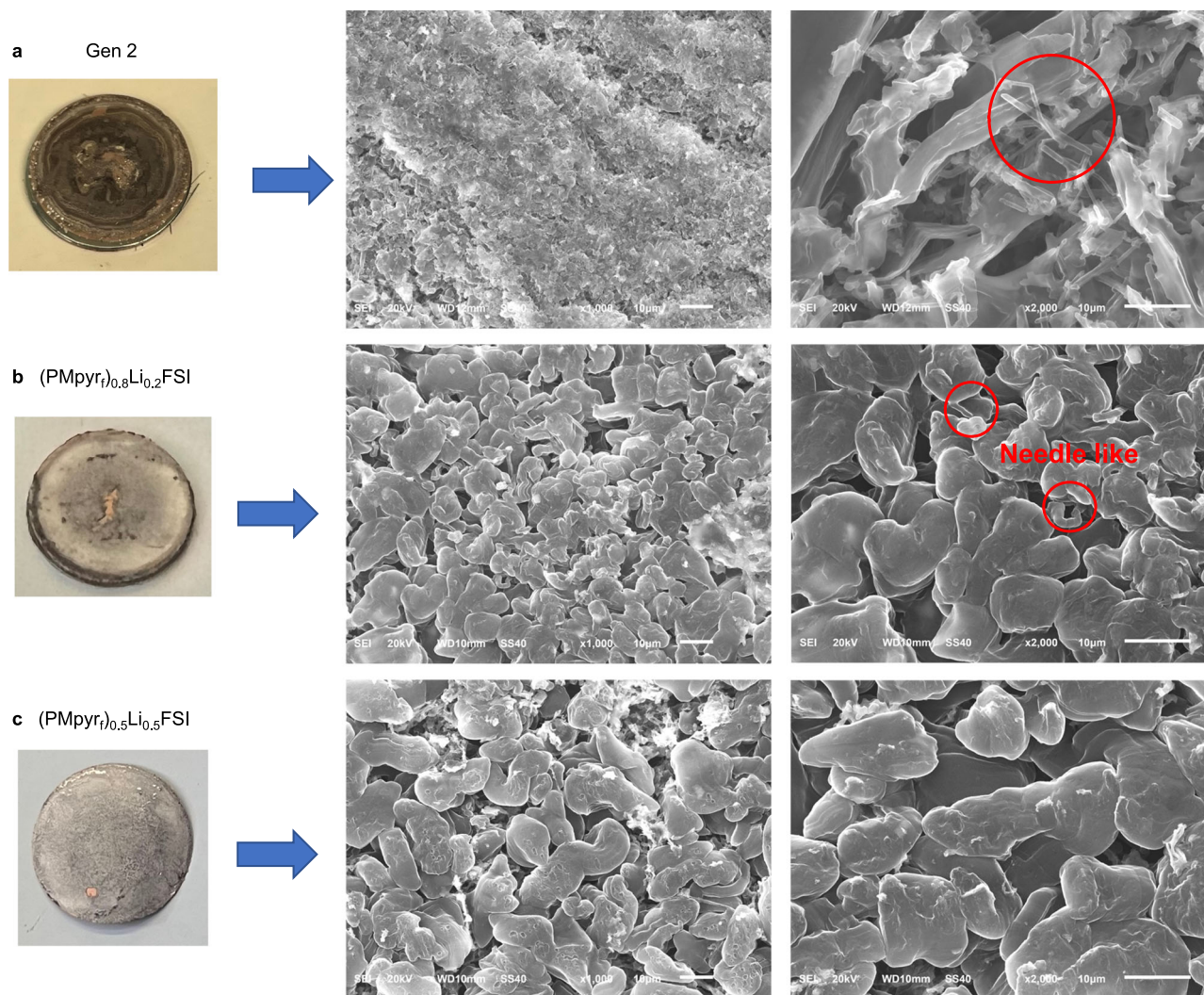


Fig. 6 | SEM of plated Li on Cu foil with current density of 0.1 mA/cm^2 . **a** Gen 2, **b** $(\text{PMpyr})_{0.8}\text{Li}_{0.2}\text{FSI}$, and **c** $(\text{PMpyr})_{0.5}\text{Li}_{0.5}\text{FSI}$ electrolytes.

wave functions of the ionic cores; and the generalized gradient approximation (GGA) PBE functional was used to account for the electron exchange-correlation effects⁵⁰. Energy cutoff of 520 eV and 440 eV was used to optimize the bulk for the Li anode and NMC cathode, respectively, and the corresponding Monkhorst-Pack k -point meshes were $8 \times 8 \times 8$ and $3 \times 3 \times 3$ ⁵¹. The periodic four layers of surface slab of Li (110) and NMC622 (100) was created using materials studio, and the length of the vacuum along the z -direction is at least 20 \AA to avoid spurious interactions between the periodic images. For NMC622 cathode surface calculations, 400 eV energy cutoff with a single Γ -point was used, while a k -point mesh of $3 \times 2 \times 1$ was used for Li anode system with the same energy cutoff. In order to correct the d -electron delocalization for Ni, Mn, and Co, the Hubbard U (GGA + U) was applied⁵². The U values for Ni, Mn, and Co are 6.34, 4.48, and 5.14 eV, respectively, which were obtained from previous works⁵³. The energy and geometries of the gas phase species were calculated by placing the molecule in a box with dimensions of $25 \times 25 \times 25 \text{ \AA}^3$. A single Γ -point was used for these calculations. For all calculations, the convergence criterion for the self-consistent iteration is $1 \times 10^{-5} \text{ eV}$; and the ionic relaxations stop when the force on each atom is less than 0.05 eV/\AA .

To evaluate the reducibility of the cation and anion of the IL with and without F-substitution, reduction potential was computed using Eq. (1)⁵⁴, where n is the number of electrons transferred during reduction and ΔG^{red} is the reaction free energy of the reduction, which

is approximately equal to the ΔE from DFT, since the reactants are strongly adsorbed and we anticipate the ΔS would be negligible. E_{H} and E_{Li} represents the reduction potentials of the absolute hydrogen electrode and Lithium electrode, which are 4.44 V and -3.05 V , respectively.

$$E_{\text{wrt Li}}^0 (\text{V}) = - \left(\frac{\Delta G^{\text{red}}}{n} + E_{\text{H}} \right) - E_{\text{Li}} \quad (1)$$

In order to explore the electronic properties of the ionic liquid with and without F-substitution, Gaussian calculations were carried out using Gaussian 09⁵⁵ simulation package with B3LYP functional and TZVP basis set^{56,57}.

Molecular dynamics (MD) simulations

All MD simulations were performed on the Cray cluster Theta of the Leadership Computing Facility at Argonne National Laboratory. The simulations were carried out in a high-performance mode with version 2.14 of NAMD⁵⁸, a greatly scalable molecular dynamic program used to render an atom-by-atom representation of biomolecules, created at the University of Illinois. All electrolyte simulations adopted GAMMP force field⁵⁹ generated through GAAMP server on Laboratory Computing Resource Center at Argonne National Laboratory. The molar ratios of each molecular species, Li^+ , FSI, and PMpyr^+ (or PMpyr_f^+) match the ratio in $(\text{PMpyr})_{0.8}\text{Li}_{0.2}\text{FSI}$, $(\text{PMpyr})_{0.8}\text{Li}_{0.2}\text{FSI}$, and $(\text{PMpyr})_{0.5}\text{Li}_{0.5}\text{FSI}$

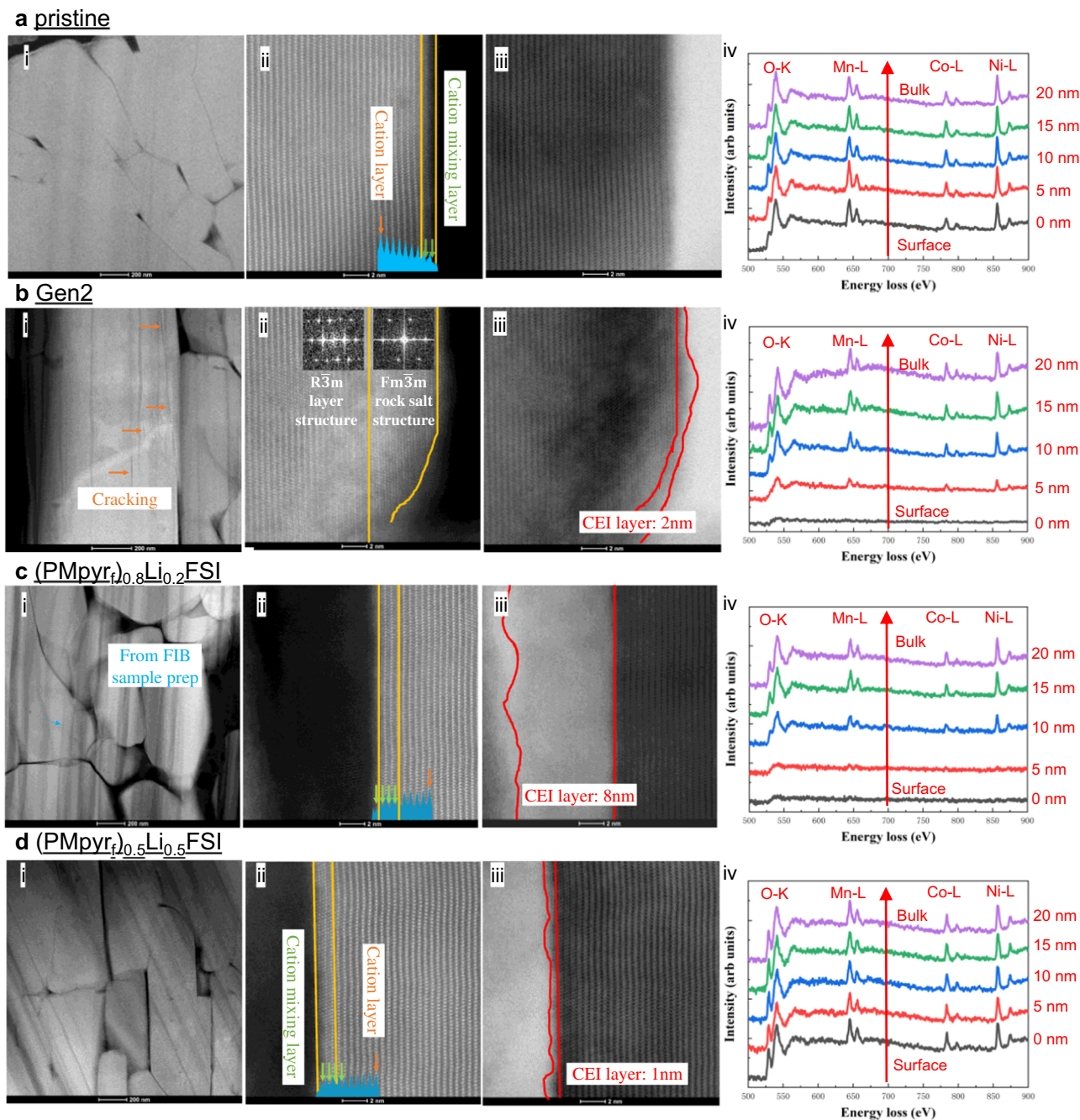


Fig. 7 | HAADF-STEM/EELS analysis of cycled NMC622 cathodes. **a** Pristine NMC622 and cycled NMC622 cathodes with different electrolytes, **b** Gen 2 electrolyte after 100 cycles, **c** (PMpyr)_{0.8}Li_{0.2}FSI electrolyte after 100 cycles, and

d (PMpyr)_{0.5}Li_{0.5}FSI electrolyte after 300 cycles. (i–ii) HAADF-STEM images, (iii) BF-STEM images, and (iv) EELS line scan from primary particle surface to bulk of cathode.

electrolytes. The composite system of the NMC622 cathode, electrolyte, and Li-metal anode are constructed and modeled with all-atom models reported in our previous study⁶⁰. The number of atoms for the simulated systems range between 418,300 and 418,600, and dimension of each simulation cell is $\sim 100 \text{ \AA} \times 100 \text{ \AA} \times 560 \text{ \AA}$, including a 125 \AA vacuum between the anode and image of the cathode to eliminate spurious long-range interactions. All simulations adopt Periodic Boundary Condition under constant NVT condition. The equations of motion were integrated with a 2 fs time step, using Langevin dynamics at a temperature of 300 K. To overcome the slow dynamics due to the high viscosity of the simulated systems, Hamiltonian simulated annealing method (HSA)⁶¹ was employed to accelerate the equilibration of MD trajectories. In each HSA simulation, 64 independent trajectories

were generated, and all of them were used to get a statistical average of structural properties. Each trajectory lasts 20 ns and the last 10 ns was adopted to do a statistical average. Snapshot of each trajectory was sampled at an interval of 100 ps, and thus for each simulated system, 6400 snapshots were adopted to guarantee high-fidelity sampling.

Data availability

Source data are provided with this paper.

References

1. Heiskanen, S. K., Kim, J. & Lucht, B. L. Generation and evolution of the solid electrolyte interphase of lithium-ion batteries. *Joule* **3**, 2322–2333 (2019).

2. Fong, R., von Sacken, U. & Dahn, J. R. Studies of lithium intercalation into carbons using nonaqueous electrochemical cells. *J. Electrochem. Soc.* **137**, 2009–2013 (1990).
3. Aiken, C. P. et al. $\text{Li}[\text{Ni}_{0.5}\text{Mn}_{0.3}\text{Co}_{0.2}]\text{O}_2$ as a superior alternative to LiFePO_4 for long-lived low voltage Li-ion cells. *J. Electrochem. Soc.* **169**, 050512 (2022).
4. Peled, E. The electrochemical behavior of alkali and alkaline earth metals in nonaqueous battery systems—the solid electrolyte interphase model. *J. Electrochem. Soc.* **126**, 2047–2051 (1979).
5. Aurbach, D., Markovsky, B., Shechter, A., Ein-Eli, Y. & Cohen, H. A comparative study of synthetic graphite and Li electrodes in electrolyte solutions based on ethylene carbonate-dimethyl carbonate mixtures. *J. Electrochem. Soc.* **143**, 3809–3820 (1996).
6. Xu, K. Nonaqueous liquid electrolytes for lithium-based rechargeable batteries. *Chem. Rev.* **104**, 4303–4418 (2004).
7. Verma, P., Maire, P. & Novák, P. A review of the features and analyses of the solid electrolyte interphase in Li-ion batteries. *Electrochim. Acta* **55**, 6332–6341 (2010).
8. Xu, K. Electrolytes and interphases in Li-ion batteries and beyond. *Chem Rev* **114**, 11503–11618 (2014).
9. Peled, E. & Menkin, S. Review—SEI: past, present and future. *J. Electrochem. Soc.* **164**, A1703–A1719 (2017).
10. Tan, J., Matz, J., Dong, P., Shen, J. & Ye, M. A growing appreciation for the role of LiF in the solid electrolyte interphase. *Adv. Energy Mater.* **11**, 2100046 (2021).
11. He, M., Guo, R., Hobold Gustavo, M., Gao, H. & Gallant Betar, M. The intrinsic behavior of lithium fluoride in solid electrolyte interphases on lithium. *Proc. Natl Acad. Sci. USA* **117**, 73–79 (2020).
12. Lu, Y., Tu, Z. & Archer, L. A. Stable lithium electrodeposition in liquid and nanoporous solid electrolytes. *Nat. Mater.* **13**, 961–969 (2014).
13. Sheng, O. et al. In situ construction of a LiF-enriched interface for stable all-solid-state batteries and its origin revealed by cryo-TEM. *Adv. Mater.* **32**, 2000223 (2020).
14. Fan, X. et al. Highly fluorinated interphases enable high-voltage Li-metal. *Batteries. Chem.* **4**, 174–185 (2018).
15. Yamada, Y., Wang, J., Ko, S., Watanabe, E. & Yamada, A. Advances and issues in developing salt-concentrated battery electrolytes. *Nat. Energy* **4**, 269–280 (2019).
16. Ren, X. et al. High-concentration ether electrolytes for stable high-voltage lithium metal batteries. *ACS Energy Lett.* **4**, 896–902 (2019).
17. Cao, X. et al. Monolithic solid–electrolyte interphases formed in fluorinated orthoformate-based electrolytes minimize Li depletion and pulverization. *Nat. Energy* **4**, 796–805 (2019).
18. Chen, S. et al. High-voltage lithium-metal batteries enabled by localized high-concentration electrolytes. *Adv. Mater.* **30**, 1706102 (2018).
19. Ren, X. et al. Enabling high-voltage lithium-metal batteries under practical conditions. *Joule* **3**, 1662–1676 (2019).
20. Chen, S. et al. High-efficiency lithium metal batteries with fire-retardant electrolytes. *Joule* **2**, 1548–1558 (2018).
21. Niu, C. et al. High-energy lithium metal pouch cells with limited anode swelling and long stable cycles. *Nat. Energy* **4**, 551–559 (2019).
22. Ren, X. et al. Localized High-concentration sulfone electrolytes for high-efficiency lithium-metal. *Batteries. Chem.* **4**, 1877–1892 (2018).
23. Cao, X. et al. Effects of fluorinated solvents on electrolyte solvation structures and electrode/electrolyte interphases for lithium metal batteries. *Proc. Natl Acad. Sci. USA* **118**, e2020357118 (2021).
24. Wang, Y. et al. An all-fluorinated electrolyte toward high voltage and long cycle performance dual-ion batteries. *Adv. Energy Mater.* **12**, 2103360 (2022).
25. Holoubek, J. et al. An all-fluorinated ester electrolyte for stable high-voltage Li metal batteries capable of ultra-low-temperature operation. *ACS Energy Lett.* **5**, 1438–1447 (2020).
26. Xue, W. et al. FSI-inspired solvent and “full fluorosulfonyl” electrolyte for 4 V class lithium-metal batteries. *Energy Environ. Sci.* **13**, 212–220 (2020).
27. Xue, W. et al. Stabilizing electrode–electrolyte interfaces to realize high-voltage $\text{Li}|\text{LiCoO}_2$ batteries by a sulfonamide-based electrolyte. *Energy Environ. Sci.* **14**, 6030–6040 (2021).
28. Xue, W. et al. Ultra-high-voltage Ni-rich layered cathodes in practical Li metal batteries enabled by a sulfonamide-based electrolyte. *Nat. Energy* **6**, 495–505 (2021).
29. Chen, L. et al. A 63 m superconcentrated aqueous electrolyte for high-energy Li-ion batteries. *ACS Energy Lett.* **5**, 968–974 (2020).
30. Zhou, L. et al. Opportunities and challenges for aqueous metal-proton batteries. *Matter* **4**, 1252–1273 (2021).
31. Zhang, H., Liu, X., Li, H., Hasa, I. & Passerini, S. Challenges and strategies for high-energy aqueous electrolyte rechargeable batteries. *Angew. Chem. Int. Ed.* **60**, 598–616 (2021).
32. Kim, K. H., Cho, J. H., Hwang, J. U., Im, J. S. & Lee, Y.-S. A key strategy to form a LiF-based SEI layer for a lithium-ion battery anode with enhanced cycling stability by introducing a semi-ionic CF bond. *J. Industrial Eng. Chem.* **99**, 48–54 (2021).
33. Sharova, V. et al. Comparative study of imide-based Li salts as electrolyte additives for Li-ion batteries. *J. Power Sour.* **375**, 43–52 (2018).
34. He, M. et al. Fluorinated electrolytes for 5-V Li-ion chemistry: probing voltage stability of electrolytes with electrochemical floating test. *J. Electrochem. Soc.* **162**, A1725–A1729 (2015).
35. Liu, Q., Hsu, C.-W., Dzwiniel, T. L., Puppek, K. Z. & Zhang, Z. A fluorine-substituted pyrrolidinium-based ionic liquid for high-voltage Li-ion batteries. *Chem. Commun.* **56**, 7317–7320 (2020).
36. Wang, C., Meng, Y. S. & Xu, K. Perspective—fluorinating interphases. *J. Electrochem. Soc.* **166**, A5184–A5186 (2018).
37. Adams, B. D., Zheng, J., Ren, X., Xu, W. & Zhang, J.-G. Accurate determination of coulombic efficiency for lithium metal anodes and lithium metal batteries. *Adv. Energy Mater.* **8**, 1702097 (2018).
38. Wood, K. N. et al. Dendrites and pits: untangling the complex behavior of lithium metal anodes through operando video microscopy. *ACS Central Sci.* **2**, 790–801 (2016).
39. Nie, K. et al. Interfaces between cathode and electrolyte in solid state lithium batteries: challenges and perspectives. *Front. Chem.* **6**, 616 (2018).
40. Heiskanen, S. K., Laszczynski, N. & Lucht, B. L. Perspective—surface reactions of electrolyte with $\text{LiNi}_x\text{Co}_y\text{Mn}_z\text{O}_2$ cathodes for lithium ion batteries. *J. Electrochem. Soc.* **167**, 100519 (2020).
41. Yang, L. et al. Harnessing the surface structure to enable high-performance cathode materials for lithium-ion batteries. *Chem. Soc. Rev.* **49**, 4667–4680 (2020).
42. Liu, W. et al. Nickel-rich layered lithium transition-metal oxide for high-energy lithium-ion batteries. *Angew. Chem. Int. Ed.* **54**, 4440–4457 (2015).
43. Lee, S. H., Hwang, J.-Y., Park, S.-J., Park, G.-T. & Sun, Y.-K. Adiponitrile (C6H8N2): a new Bi-functional additive for high-performance Li-metal batteries. *Adv. Funct. Mater.* **29**, 1902496 (2019).
44. Andersson, A. M. et al. Surface characterization of electrodes from high power lithium-ion batteries. *J. Electrochem. Soc.* **149**, A1358 (2002).
45. Jung, S.-K. et al. Understanding the degradation mechanisms of $\text{LiNi}_{0.5}\text{Co}_{0.2}\text{Mn}_{0.3}\text{O}_2$ cathode material in lithium ion batteries. *Adv. Energy Mater.* **4**, 1300787 (2014).
46. Zheng, J. et al. Ni/Li disordering in layered transition metal oxide: electrochemical impact, origin, and control. *Acc. Chem. Res.* **52**, 2201–2209 (2019).
47. Cha, H. et al. Boosting reaction homogeneity in high-energy lithium-ion battery cathode materials. *Adv. Mater.* **32**, 2003040 (2020).

48. Kresse, G. & Furthmüller, J. Efficient iterative schemes for ab initio total-energy calculations using a plane-wave basis set. *Phys. Rev. B* **54**, 11169–11186 (1996).
49. Blochl, P. E. Projector augmented-wave method. *Phys. Rev. B* **50**, 17953–17979 (1994).
50. Perdew, J. P., Burke, K. & Ernzerhof, M. Generalized gradient approximation made simple. *Phys. Rev. Lett.* **77**, 3865–3868 (1996).
51. Monkhorst, H. J. & Pack, J. D. Special points for Brillouin-zone integrations. *Phys. Rev. B* **13**, 5188–5192 (1976).
52. Anisimov, V. I., Zaanen, J. & Andersen, O. K. Band theory and Mott insulators—Hubbard-U instead of Stoner-I. *Phys. Rev. B* **44**, 943–954 (1991).
53. Xu, S. Z. et al. Ab initio modeling of electrolyte molecule ethylene carbonate decomposition reaction on Li(Ni,Mn,Co)O₂ cathode surface. *ACS Appl. Mater. Inter.* **9**, 20545–20553 (2017).
54. Kang, J., Kim, K. C. & Jang, S. S. Density functional theory modeling-assisted investigation of thermodynamics and redox properties of boron-doped corannulenes for cathodes in lithium-ion batteries. *J. Phys. Chem. C* **122**, 10675–10681 (2018).
55. Gaussian 16 Rev. C.01, Frisch, M. J. et al., Gaussian, Inc., Wallingford, CT, 2016.
56. Becke, A. D. Density-functional thermochemistry.3. The role of exact exchange. *J. Chem. Phys.* **98**, 5648–5652 (1993).
57. Schafer, A., Huber, C. & Ahlrichs, R. Fully optimized contracted Gaussian-basis sets of triple zeta valence quality for atoms Li to Kr. *J. Chem. Phys.* **100**, 5829–5835 (1994).
58. Phillips, J. C. et al. Scalable molecular dynamics with NAMD. *J. Comput. Chem.* **26**, 1781–1802 (2005).
59. Huang, L. & Roux, B. Automated force field parameterization for nonpolarizable and polarizable atomic models based on ab initio target data. *J. Chem. Theory Comput.* **9**, 3543–3556 (2013).
60. Liu, Q., Jiang, W., Yang, Z. & Zhang, Z. An environmentally benign electrolyte for high energy lithium metal batteries. *ACS Appl. Mater. Interfaces* **13**, 58229–58237 (2021).
61. Jiang, W. Accelerating convergence of free energy computations with Hamiltonian simulated annealing of solvent (HSAS). *J. Chem. Theory Comput.* **15**, 2179–2186 (2019).

Acknowledgements

This work was funded by the U.S. Department of Energy (DOE), Office of Energy Efficiency and Renewable Energy, Vehicle Technologies Office. Support from Tien Duong, Peter Faguy and Mallory Clites of Vehicle Technology Office is gratefully acknowledged. This research used the Leadership Computing Facility resource at Argonne National Laboratory, which is supported by DOE Office of Science under Contract No. DE-AC02-06CH11357. TEM/EELS were performed using EMSL (grid.436923.9), a DOE Office of Science User Facility sponsored by the Office of Biological and Environmental Research located at Pacific Northwest National Laboratory (PNNL). The submitted manuscript has

been created by UChicago Argonne, LLC, Operator of Argonne National Laboratory.

Author contributions

Z.Z. and K.X. conceived the idea and proposed the research. Q.L. designed experiments, performed the electrochemical measurements, characterized materials and analyzed the data. K.P. synthesized the MeFSI. W.J. performed the molecular dynamics simulations. J.X., D.-J.Y., and C.L. performed the DFT calculations. Y.X. and C.W. performed the TEM/EELS analysis. Z.Y. performed the XPS measurement. K.X. and Z.Z. contributed to the discussion and provided suggestions. Q.L., W.J., K.X., and Z.Z. wrote the manuscript with inputs from all other co-authors.

Competing interests

The authors declare no competing interests.

Additional information

Supplementary information The online version contains supplementary material available at <https://doi.org/10.1038/s41467-023-38229-7>.

Correspondence and requests for materials should be addressed to Kang Xu or Zhengcheng Zhang.

Peer review information *Nature Communications* thanks Yan Zhao, and the other, anonymous, reviewers for their contribution to the peer review of this work. Peer reviewer reports are available.

Reprints and permissions information is available at <http://www.nature.com/reprints>

Publisher's note Springer Nature remains neutral with regard to jurisdictional claims in published maps and institutional affiliations.

Open Access This article is licensed under a Creative Commons Attribution 4.0 International License, which permits use, sharing, adaptation, distribution and reproduction in any medium or format, as long as you give appropriate credit to the original author(s) and the source, provide a link to the Creative Commons license, and indicate if changes were made. The images or other third party material in this article are included in the article's Creative Commons license, unless indicated otherwise in a credit line to the material. If material is not included in the article's Creative Commons license and your intended use is not permitted by statutory regulation or exceeds the permitted use, you will need to obtain permission directly from the copyright holder. To view a copy of this license, visit <http://creativecommons.org/licenses/by/4.0/>.

© UChicago Argonne, LLC, Operator of Argonne National Laboratory 2023